

Article

Suppression of Wind Generator Speed Vibration Based on the Internal Model Control with Three Degrees of Freedom

Chenyang Zhou and Yanxia Shen *

School of Things Internet Engineering, Jiangnan University, Wuxi 214122, China

* Correspondence: shenyx@jiangnan.edu.cn

Abstract: When the wind power system is working in the maximum wind energy tracking area, or when its mechanical drivetrain system vibrates and the vibration frequency is relatively high, the system cannot suppress the speed vibration of the generator in the drivetrain system by adjusting the pitch angle. In this paper, a generator speed control system based on the three degrees of freedom internal model control (3-DOF-IMC) is established to control the generator speed. Thus, a scheme of using the feedback filter in the 3-DOF-IMC to suppress generator speed vibration caused by drivetrain shaft elasticity and gear clearance in the drivetrain system is proposed. Firstly, the vibration problem and waveform of the two-mass wind power drivetrain systems are discussed, and the generator's vector control and speed control systems are analyzed. Secondly, the principle of the 3-DOF-IMC is described, and the influence of the three controllers on the speed tracking performance and anti-interference performance of the generator is discussed. The suppression ability of the feedback filter for different forms of disturbance signals is emphasized. Finally, the feedback filter controls the generator speed and eliminates the influence of drivetrain vibration on the generator speed. To verify the superiority of the proposed method, the vibration suppression effect, tracking performance and anti-interference performance of the proposed method are compared with the engineering design method (EDM) and conventional IMC (1-DOF-IMC) method. When the parameter $\alpha/\beta = 0.66$, the generator speed amplitude overshoot of the proposed method is the same as the EDM. When $\alpha/\beta = 1$, it is only 4% of the amplitude overshoot of the EDM. In addition, the tracking performance and anti-interference performance of the proposed method can be adjusted independently, and it is better than the EDM and the 1-DOF-IMC method.

Keywords: wind power system; three degrees of freedom internal model control (3-DOF-IMC); generator speed control; anti-interference



Citation: Zhou, C.; Shen, Y.

Suppression of Wind Generator Speed Vibration Based on the Internal Model Control with Three Degrees of Freedom. *Energies* **2022**, *15*, 7445. <https://doi.org/10.3390/en15197445>

Academic Editor: Armando Pires

Received: 10 September 2022

Accepted: 28 September 2022

Published: 10 October 2022

Publisher's Note: MDPI stays neutral with regard to jurisdictional claims in published maps and institutional affiliations.



Copyright: © 2022 by the authors. Licensee MDPI, Basel, Switzerland. This article is an open access article distributed under the terms and conditions of the Creative Commons Attribution (CC BY) license (<https://creativecommons.org/licenses/by/4.0/>).

1. Introduction

The wind turbine, gearbox, generator, and drivetrain shaft constitute the wind power drivetrain system. The essence of vibration in the wind drivetrain system is caused by the torque difference between the wind turbine's pneumatic torque and the generator's electromagnetic torque [1]. The main method for suppressing the vibration of the wind drivetrain system is reducing the torque difference by adjusting the pitch angle of the wind turbine or by controlling the electromagnetic torque of the generator.

There are two specific suppression methods. In the first method, a mechanical drivetrain system based on the wind power system adjusts the aerodynamic torque of the wind turbine through variable pitch control. In the second method, the generator is controlled by adjusting its electromagnetic torque. The vibration frequency caused by the elasticity of the drivetrain shaft is relatively low in the wind mechanical drivetrain system. The pitch-speed closed loop of the wind power system can be used to suppress the speed vibration of the generator. However, the vibration frequency caused by gear clearance is still high [2,3], and the variable pitch actuator cannot keep up with the rapid changes imposed by the variable

pitch control. Therefore, the torque-speed closed loop of the wind power system can be used to control the generator torque and eliminate its speed vibration [4].

The existing research on the vibration and suppression of wind power systems is usually focused on the drivetrain system. For example, the mathematical model of the wind mechanical drivetrain system was discussed in [5]. The authors established the mathematical model of the wind drivetrain for different mass blocks according to the equivalent mass block method. Combined with a doubly fed generator, the influence of the drivetrain parameters on the transient characteristics and stability of wind turbines was also researched. In Ref. [6], the authors analyzed the influence of wind drivetrain oscillations on the life and stability of drivetrain shafting for the doubly fed wind generator. Moreover, it was pointed out that increasing the electrical damping could effectively suppress shafting oscillation. The authors concluded that the amplitude of the shafting oscillation could be suppressed by increasing the electrical stiffness.

The equivalent mass block method was adopted in [7] to establish the equivalent model of the three-mass wind power system. The influence of the blade-to-hub ratio on the transient stability of a large wind turbine was analyzed. The results showed that blade stiffness parameters and the blade-to-hub inertia ratio significantly impact the transient stability of a wind power system. Three equivalent drivetrain system models of the wind power system were established in [8]. According to the obtained results, when the drivetrain shaft is disturbed, the wind drivetrain system produces a large torque, resulting in torsional vibration between the parts of the drivetrain shaft system.

The vibration of the wind power system originates from various sources, such as the blades, gearbox clearance, and generator vibration due to bearing failure [9]. The authors investigated the negative effect of gear clearance vibration on the performance of wind power systems. In addition, an effective method of controlling the vibration of the wind power system was also explored.

The drivetrain vibration of the wind power system can easily cause blade damage [10]. Hence, in [10], the control strategy was introduced to suppress wind drivetrain vibration, and a damping controller for the blade vibration of the wind drivetrain was designed.

Reference [11] studied the mechanism of the wind power drivetrain torsional vibration, and the impact rules of different parameters on the damping of torsional vibration in the drivetrain were investigated in detail. In Ref. [12], the wind speed, turbine, shaft system and generator were modeled, respectively, and grid disturbances on the shafting oscillation were verified. Reference [13] focused on wind turbine drivetrains and reviewed the vibration and noise from a systematic perspective of “generation–analysis–reduction”. Reference [14] revealed the essential vibration characteristics, and a dynamic model of the drivetrain of the doubly fed wind turbine was established by adopting the lumped parameter method; the torsional vibrations of the generator, gears and wind wheel were considered. In Ref. [15], the coupled dynamic model of the translation torsion of the main drive system of a wind turbine was built by the lumped parameter method, then the time-varying meshing stiffness of each gear pair was simulated by Fourier series and by considering the internal excitations caused by bearing support stiffness, torsional shaft stiffness, and the external excitation caused by the time-varying wind speed.

According to the characteristics of the multi-frequency and time-varying coupling of the tower vibration of a large-scale wind turbine, in [16], a parallel adaptive notch filter based on driven knowledge was proposed to track the multi-frequency of the tower vibration online and to eliminate the influence of the vibration components of each frequency. Reference [17] summarized the research results of the related vibration control methods and vibration-reduction devices, and forecasted the research trend of tower vibration control in the future. Reference [18] revealed the influence of the wind farm type and the operating conditions of the shaft system of the synchronous generator set, and the mechanism of torsional vibration. Reference [19] comprehensively reviewed the latest progress and new trends of wind power drivetrain vibration control and summarized the research on drivetrain vibration control before 2020. According to the conducted literature review, it can be

concluded that most of the relevant research has investigated the mechanical drivetrain system and tower of the wind power system. Lastly, it can also be concluded that the stability and vibration of the drivetrain system significantly affect the performance of the wind power system.

The pitch control actuator cannot respond to a rapid change in the controller due to the high-frequency vibration caused by the gear clearance of the wind drivetrain system. Moreover, when the wind power system operates in the maximum wind energy tracking area, the wind power system adopts a fixed pitch control. Consequently, the vibration of the wind drivetrain system cannot be suppressed by adjusting the pitch angle.

Hence, the generator's electromagnetic torque or speed vibration can be eliminated by controlling the generator. Drivetrain and generator vibration is reflected in the vibration of the output speed or generator torque. Therefore, suppressing the vibration of the wind power system can be achieved by controlling the generator's output speed.

The doubly fed generator is a nonlinear, strongly coupled, multivariable high-order system controlled by either a vector control or direct torque control. After vector transformation, the doubly fed generator needs to be decoupled due to the cross-coupling problem [20,21]. The doubly fed generator requires excellent tracking and anti-interference performance. Moreover, it is beneficial if the abovementioned performances can be adjusted independently. In addition, the mechanical resonance caused by drivetrain shaft elasticity and gear clearance exists in the drivetrain system. Resonance increases the difficulty of an accurate mathematical description of the controlled object, resulting in model uncertainty in the wind power system. This model uncertainty is caused by mechanical resonance and is often described by multiplicative perturbation [22]. Therefore, it is necessary to establish a control method that can independently adjust the generator's tracking and anti-interference performance. Furthermore, the method should also be characterized by a robust performance regarding the model uncertainty caused by mechanical resonance. In other words, the three degrees of freedom internal model control (3-DOF-IMC) method can be used to solve the above problems.

In this paper, the vibration suppression problem of the wind drivetrain system is briefly explained, the vibration principle and suppression method are analyzed, and the existing problems are discussed. Secondly, the mathematical model of a doubly fed generator is analyzed, the decoupling method of the generator's cross-coupling current is provided, and the design method of current and speed loops is discussed. Finally, the 3-DOF-IMC principle [23] is analyzed, and the tracking and anti-interference performances of generator speed based on the 3-DOF-IMC are discussed. Moreover, the uncertainty of the controlled object caused by the mechanical resonance is analyzed, and the filter's performance regarding the robust control and uncertain suppression is discussed. Finally, the simulation method is employed to demonstrate the effectiveness of the abovementioned methods.

2. Vibration Suppression and Existing Problems of a Wind-Powered Mechanical Drivetrain System

The wind turbine, gearbox, and generator are the three most fundamental components of the wind drivetrain, and the gearbox contains multiple gears and clearances. According to different research purposes, different mass block models can be established for the drivetrain. The centralized mass block (one mass) model is too simple to accurately reflect the actual dynamic performance of the drivetrain. Although the three-mass model is more accurate but complex, the mathematical model is not convenient to transform. To highlight the influence of the application of a novel control strategy for suppressing drivetrain vibration with clearance, a typical two-mass model was selected as the research object for the wind drivetrain analysis. The reasons are as follows: (1) the multi-mass system containing M mass blocks is composed of $M-1$ two-mass systems, with the two-mass system serving as the basis. (2) The research conclusions of the two-mass system can be extended to the multi-mass system. When using the two-mass model, it is necessary to carry out

the necessary gearbox equivalence and conversion of the gearbox's rotational inertia and elastic coefficient.

In addition, the wind turbine's PID control cannot suppress the vibration resulting from gear clearance. Therefore, the electromagnetic torque or speed of the wind generator can be controlled by the torque-speed closed loop to eliminate the wind drivetrain vibration with clearance.

2.1. Composition and Model of Two-Mass Wind-Powered Mechanical Drivetrain System

Figure 1 depicts a schematic diagram of the wind drivetrain system composition for a doubly fed wind-powered system [24]. The doubly fed generator is connected to the drivetrain system via a high-speed shaft. Thus, the drivetrain system's performance affects the generator's output performance. In addition, the generator is connected to the grid through the transformer, while the generator's electrical control system controls the converter that regulates the electromagnetic torque and speed of the generator. A doubly fed wind generator is one of the core components of the wind-powered system. The vibration of the drivetrain system causes uncertainty in the generator model, which increases the controlling difficulty of the electric drivetrain system.

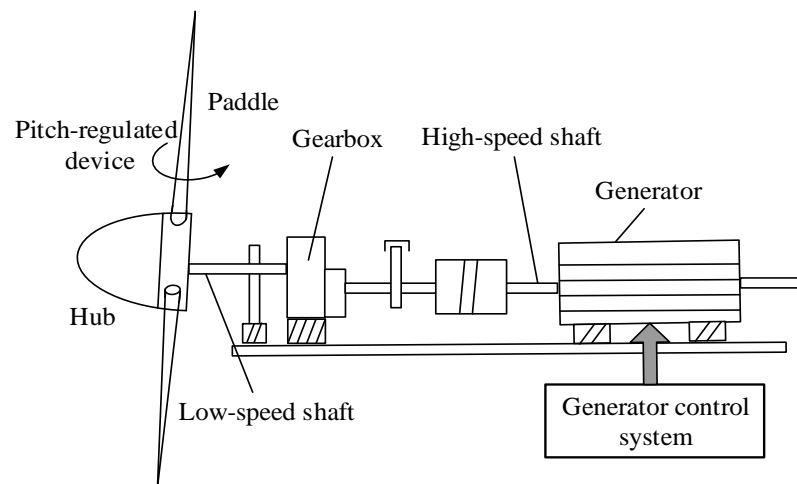


Figure 1. A schematic diagram of the wind power system.

The gearbox in Figure 1 is regarded as an equivalent gear. The mass of the driving gear is converted to the wind turbine side, and the mass of the driven gear is converted to the generator side. The gear clearance influence of the three-stage gear system in the gearbox is represented by an equivalent total clearance to ensure that a two-mass drivetrain model with gear clearance can be obtained (Figure 2).

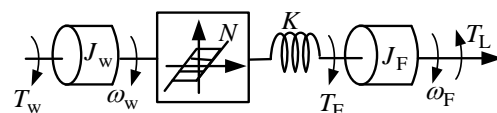


Figure 2. A schematic diagram of the mechanical structure of the two-mass wind drivetrain.

In Figure 2, T_W is the driving torque of the wind turbine, T_F is the rotational torque of the generator, T_L is the load resistance torque, ω_W is the wind turbine rotation speed, ω_F is the generator rotation speed, J_W is the equivalent moment of inertia of the wind turbine mass block (including the converted value of the rotational inertia of the driving gear), J_F is the equivalent moment of inertia of the generator mass block (including the converted value of the rotational inertia of the driven gear), and K is the equivalent elastic coefficient of the wind drivetrain that includes the converted elastic coefficient of the gearbox. Lastly, the clearance module N represents the total equivalent clearance of the gearbox.

2.2. Mathematical Model of the Two-Mass Wind Turbine Drivetrain

The gear clearance is not considered in Figure 2. First, Equation (1) can be obtained. Then, the Laplace transform of Equation (1) is used to obtain Equation (2):

$$\begin{cases} T_W - T_F = J_W \frac{d\omega_W}{dt} \\ T_F = K \int (\omega_W - \omega_F) dt, \\ T_F - T_L = J_F \frac{d\omega_F}{dt} \end{cases} \quad (1)$$

$$\begin{cases} J_W \omega_W s = T_W - T_F \\ T_F = \frac{K}{s} (\omega_W - \omega_F) . \\ J_F \omega_F s = T_F - T_L \end{cases} \quad (2)$$

After obtaining the transfer function structure diagram of the wind drivetrain, the non-linear clearance unit N is added according to Equation (2). The transfer function structure diagram of the two-mass wind drivetrain with gear clearance is shown in Figure 3a. The input/output characteristics of gear clearance are depicted in Figure 3b, and the mathematical model is shown in Equation (3).

$$q = \begin{cases} k(v - b) ; \frac{dq}{dt} > 0 \\ k(v + b) ; \frac{dq}{dt} < 0 , \\ q_m \text{sgn}(v) ; \frac{dq}{dt} = 0 \end{cases} \quad (3)$$

where the input is the position v of the equivalent driving gear, the output is the position q of the driven gear, $2b$ is the total gear clearance, and K is the characteristic slope.

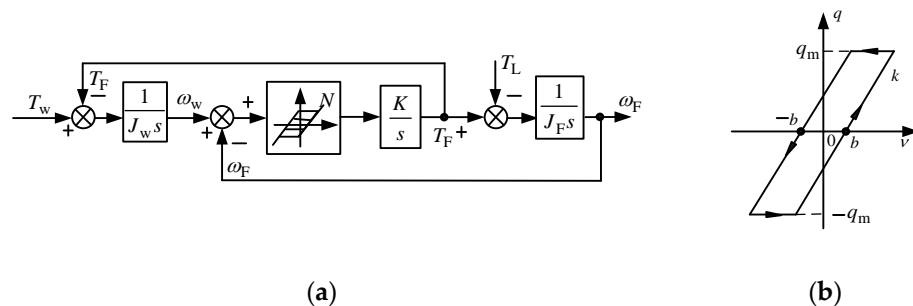


Figure 3. The transfer function structure diagram of the two-mass wind drivetrain with clearance: (a) the transfer function structure diagram of the two-mass wind drivetrain with clearance; (b) non-linear characteristics of gear clearance.

2.3. Wind Drivetrain Vibration Analysis and Suppression

In the wind drivetrain system shown in Figure 1, the elasticity of the drive shaft and gear clearance of the gearbox causes the vibration of the drivetrain system and the electromagnetic torque or speed of the generator.

2.3.1. Elastic Vibration Analysis of a Two-Mass Wind Drivetrain

The generator speed for the rotational torque T_W is ω_W . Thus, Equation (4) can be obtained as follows:

$$\frac{\omega_W}{T_W} = \frac{K}{J_W J_F s^3 + (J_W + J_F) K s} \quad (4)$$

According to Equation (4), a resonant point in the drivetrain [25] indicates that vibration exists, and the resonant frequency is $\omega_r = \sqrt{\frac{J_W + J_F}{J_W J_F}} K$. In Equation (4), the parameter in

Table 1 [5] is substituted to obtain the resonant frequency as $\omega_r = 0.863 \left(\frac{\text{rad}}{\text{s}} \right)$, which is a relatively low vibration frequency.

Table 1. Parameters of the experimental simulation.

No	Parameter	Value
1	J_W (kg·m ²)	2.6
2	J_F (kg·m ²)	0.776
3	K (n·m/rad)	0.452
4	2b (rad)	0.4

2.3.2. Vibration Analysis of Gear Clearance for a Two-Mass Wind Drivetrain

The system output of the same parameters without clearance is subtracted from the output of the two-mass wind drivetrain transfer function based on Figure 3a. Thus, an experimental system capable of verifying clearance vibration is created, as shown in Figure 4a. The speed deviation $\Delta\omega_F$ between the two output speed waveforms, which represent the vibration generated by the nonlinear gear clearance unit, is shown in Figure 4b.

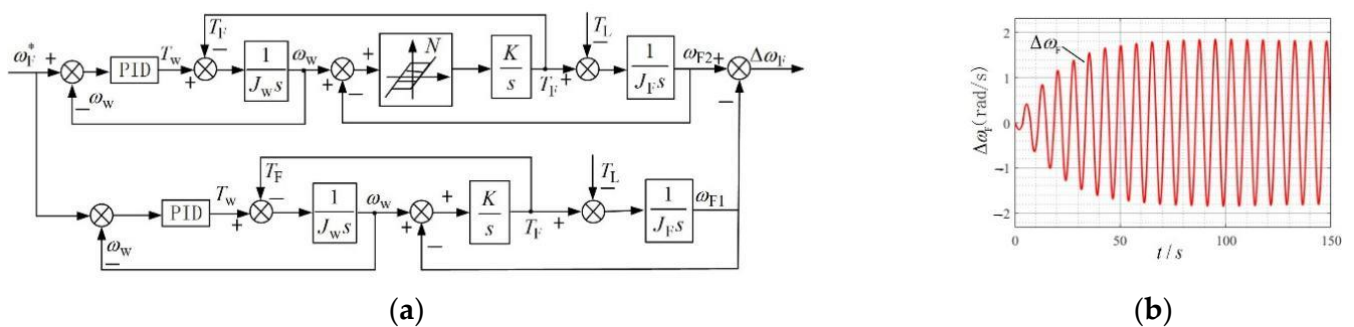


Figure 4. Experimental verification of the clearance vibration and vibration waveform: (a) experimental verification of the clearance vibration; (b) speed deviation waveform caused by clearance. * means the reference value.

2.4. Vibration Suppression Strategy

The vibration frequency caused by the elasticity of the drivetrain shaft is relatively low. As such, it can be suppressed by the wind turbine’s PID speed closed-loop control and the variable pitch of the wind power system. The speed wave of the generator after suppression is denoted as $\Delta\omega_{F1}$, as shown in Figure 5a. However, the wind turbine’s PID control cannot suppress the vibration resulting from gear clearance $\Delta\omega_{F2}$, as shown in Figure 5b. Furthermore, the vibration frequency caused by gear clearance is relatively high [2,3,26]. If variable pitch control is employed, then the variable pitch actuator cannot follow the controller’s signal to change rapidly. Therefore, the electromagnetic torque or speed of the wind generator can be controlled by the torque-speed closed loop to eliminate the wind drivetrain vibration.

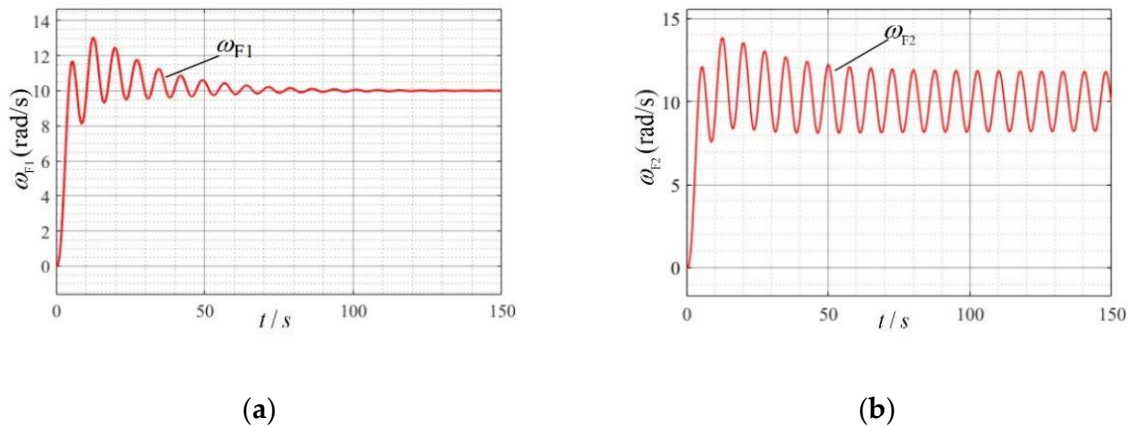


Figure 5. Vibration and suppression of the two-mass wind drivetrain with clearance: (a) vibration and elasticity suppression; (b) vibration of the gear clearance.

3. Velocity Vector Control of a Doubly Fed Wind Generator

A doubly fed induction generator (DFIG) is a nonlinear multivariable system with a high order and strong coupling. The conventional control method is not only complicated but also ineffective. Vector control can simplify the control method and obtain the same control effect as a DC motor in some aspects. At present, the research on vector control in an AC motor has made a lot of achievements and has been widely used in production, but the application of vector control technology in a generator is still in the research stage [24]. The vector control of an AC motor mainly adopts the rotor flux orientation, and the vector control of a DFIG adopts the stator flux orientation.

3.1. The Mathematical Model of a Doubly Fed Wind Generator Vector Control Based on the Stator Flux Orientation

A doubly fed generator usually adopts a vector control method to achieve the torque component of the current and excitation component decoupling control of a doubly fed generator. An asynchronous rotating d - q coordinate system model based on the stator flux orientation can be used while assuming a negligible effect of the doubly fed generator stator resistance. Under this condition, the voltage and current of a doubly fed generator can be derived as follows:

$$\begin{bmatrix} u_{d1} \\ u_{q1} \\ u_{d2} \\ u_{q2} \end{bmatrix} = \begin{bmatrix} R_s + pL_s & -\omega_s L_s & pL_m & -\omega_s L_m \\ \omega_s L_s & R_s + pL_s & \omega_s L_m & pL_m \\ pL_m & -\Delta\omega_r L_m & R_r + pL_r & -\Delta\omega_r L_r \\ \Delta\omega_r L_m & pL_m & \Delta\omega_r L_r & R_r + pL_r \end{bmatrix} \begin{bmatrix} i_{d1} \\ i_{q1} \\ i_{d2} \\ i_{q2} \end{bmatrix}, \tag{5}$$

where $\Delta\omega_r$ is the deviation of the angular frequency of a doubly fed generator, i.e., $\Delta\omega_r = \omega_s - \omega_r$, ω_s is the rotating magnetic field that synchronizes the angular frequency, and ω_r is the angular frequency of the rotor speed. The parameters R_s and R_r are the stator and rotor resistances, respectively, and L_s , L_r , and L_m are the stator inductance, rotor self-inductance, and mutual inductance between stator and rotors, respectively. The parameters u_{d1} , u_{q1} , u_{d2} , and u_{q2} are the d - and q -axis components of the stator and rotor voltages; i_{d1} , i_{q1} , i_{d2} , i_{q2} are the d - and q -axis components of the stator and rotor currents; ψ_{d1} , ψ_{q1} , ψ_{d2} , ψ_{q2} are the d - and q -axis components of the stator and rotor flux; p is the differentiation operator.

After transformation, the state equation of the rotor voltage can finally be obtained as follows:

$$\begin{cases} u_{d2}(s) - \frac{L_m^2}{L_s} \frac{di_{m1}}{dt} = (R_r + \sigma L_r s) i_{d2}(s) - \Delta\omega_r \sigma L_r i_{q2}(s) \\ u_{q2}(s) - \Delta\omega_r \frac{L_m^2}{L_s} i_{m1} = (R_r + \sigma L_r s) i_{q2}(s) + \Delta\omega_r \sigma L_r i_{d2}(s) \end{cases} \quad (6)$$

where σ is the total magnetic leakage coefficient equal to $\sigma = 1 - L_m^2/L_s L_r$, and i_{m1} is the stator excitation current.

In Equation (6), the second term on the left of the equal sign of the two equations is the constant related to the stator flux that can be regarded as a disturbance of the system and is compensated by the controller. The compensations terms added to the controller are $\frac{L_m^2}{L_s} \frac{di_{m1}}{dt}$ and $\Delta\omega_r \frac{L_m^2}{L_s} i_{m1}$. The dynamic structure of the wind generator’s rotor current after the disturbance term is offset by the controller’s compensation as shown in Figure 6.

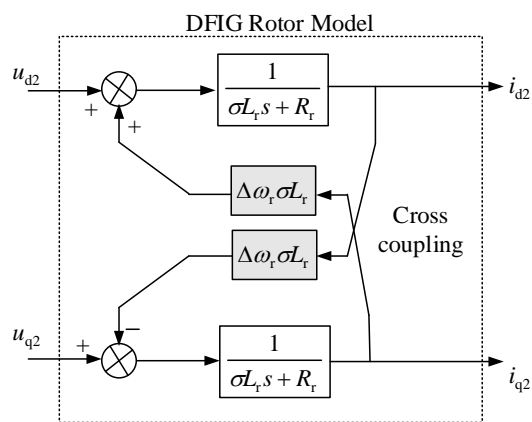


Figure 6. Dynamic structure diagram of DFIG in synchronous rotation d - q coordinate system.

A cross-coupling term between the d -axis and q -axis components of the rotor current in the generator can be seen in Figure 6. This indicates that the two components cannot be independently adjusted and affects the electromagnetic torque and speed performance of the generator. Hence, it is necessary to decouple the cross-coupling of the wind generator.

3.2. IMC Decoupling of Cross-Coupling Voltage of a Doubly Fed Wind Generator

The common decoupling methods of cross-coupled voltage include voltage feedforward decoupling, diagonal matrix decoupling, and voltage feedback decoupling. The decoupling effect of the methods mentioned above depends on the accurate mathematical model of the controlled object and the stability of the parameters. The IMC does not overly depend on the accurate mathematical model of the controlled object. Moreover, the IMC has few model accuracy requirements. Thus, it can be easily achieved in engineering. In this section, the conventional IMC decoupling method is adopted. The structure diagram that implements this decoupling control is shown in Figure 7.

(1) Theoretical analysis.

When the controlled object matches the forecast model, i.e., $G(s) = \hat{G}(s)$, the two components of the rotor current are decoupled [20].

(2) Simulation experiments.

The following parameters of the wind generator required for simulation are obtained from Table 7-3 in [24]. The rotor resistance $R_r = 0.1442 \Omega$, the rotor inductance $L_r = 35.7 \text{ mH}$, and the calculated parameters $\Delta\omega_r \sigma L_r = 0.35 \Omega$. The simulation model was built according to Figure 7. The provided input value i_{d2}^* jumped from 0 A to 5.1 A at $t = 1 \text{ s}$, and i_{q2}^* from 0 A to 5.1 A at $t = 1.5 \text{ s}$. The following can be proven:

- (1) When the inductance and resistance parameters of the wind generator rotor increase, decrease or remain constant in the same proportion, the cross-coupled voltage can achieve full decoupling by the 1-DOF-IMC, and the corresponding decoupling effect is good.
- (2) When the wind generator’s rotor inductance and resistance parameters change in different proportions and reverse directions, the cross-coupled voltage cannot achieve full decoupling by the 1-DOF-IMC due to few adjustable parameters. However, the cross-coupled voltage can achieve full decoupling by the 3-DOF-IMC. Limited by the length of the paper, the corresponding discussion will not be carried out.

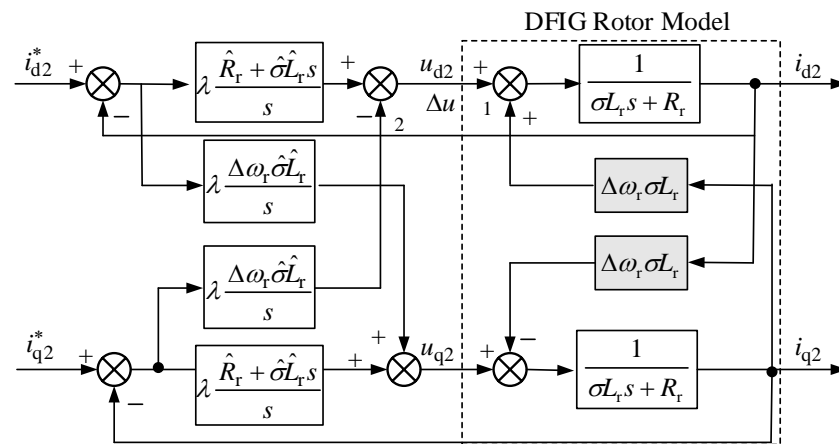


Figure 7. The block diagram of 1-DOF-IMC decoupling for DFIG. * means the reference value.

4. Design of Control System for a Doubly Fed Generator

The electric control system of a doubly fed wind generator usually adopts a speed and current double closed-loop structure. The inner current loop is designed first, followed by the outer speed loop. Generally, the inner current loop is designed as a “second-order optimal system” of the EDM to improve its dynamic performance. The 3-DOF-IMC method is used to design various controllers for the speed loop that represent the performance of the speed-regulating system. Thus, the speed loop’s tracking, anti-interference, and robustness performances can be flexibly adjusted.

In addition, the EDM is also used to design the speed loop, and it is compared with the system designed by the 3-DOF-IMC.

4.1. Design of the Rotor’s Current Control System for a Doubly Fed Generator

According to the rotor’s current control block diagram shown in Figure 7, the *d*- and *q*-axis channels of the inner current loop are completely independent after decoupling and have the same structure. Therefore, the two current controllers are the same, and only a single controller needs to be designed. The simplified dynamic structure of the rotor current loop of a doubly fed generator is shown in Figure 8. Equation (7) represents the current feedback filtering unit, β is the current feedback coefficient, and T_{oi} is the filtering time constant. Usually, a filter unit is also added to a given part of the current.

$$W_{if}(s) = \frac{\beta}{T_{oi}s + 1}, \tag{7}$$

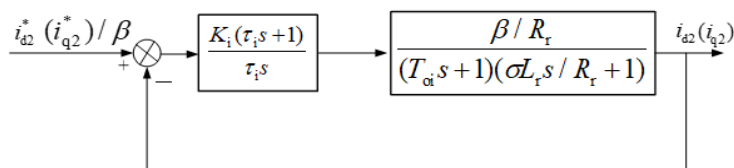


Figure 8. Simplified dynamic structure of the rotor’s current loop of the DFIG. * means the reference value.

The current loop is designed according to the “second-order optimal system” method, and the obtained current controller ACR is a PI controller:

$$W_{ACR}(s) = k_i \frac{\tau_i s + 1}{\tau_i s} \tag{8}$$

The transfer function of the current loop is approximated to an inertial unit with a small time constant via the closed-loop control of the rotor current:

$$W_{icl}(s) \approx \frac{1}{2T_{oi}s + 1} \tag{9}$$

An important function of inner current loop control is transforming the controlled object and accelerating the current tracking.

4.2. Design of Rotor Speed Control System for a Doubly Fed Generator

The reactive power control channel usually adopts a single closed-loop control to ensure that the wind generator captures the maximum wind energy. This is achieved by controlling the current of the *d*-axis of the rotor within the *d*-*q* coordinate system of the synchronous rotation of two phases. The speed control channel adopts a double closed-loop control. The inner loop is the current loop of the doubly fed generator rotor, which is achieved by controlling the current of the *q*-axis of the rotor. The outer loop is the generator speed loop. The block diagram of a doubly fed generator’s complete rotor electrical control system is shown in Figure 9.

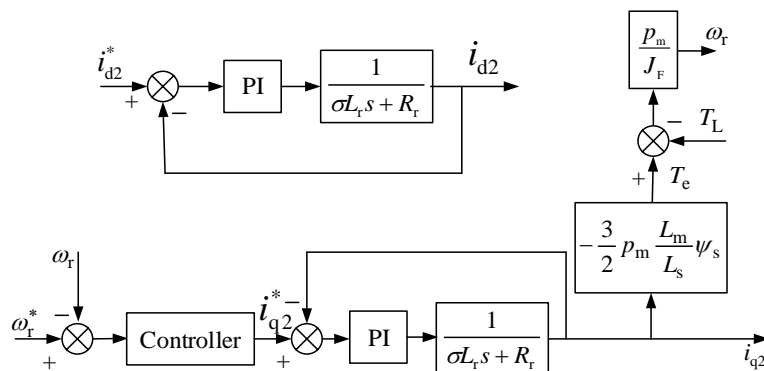


Figure 9. Complete block diagram of the rotor control system of a DFIG. * means the reference value.

- (1) The controlled object of the speed loop

The simplified rotor inner current loop, i.e., Equation (9), is substituted into Figure 9. After further simplification, the dynamic structure diagram of the speed loop is shown in Figure 10.

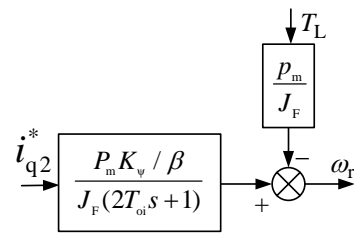


Figure 10. Simplified structure of a speed-loop-controlled object. * means the reference value.

The declaring constants can be expressed as follows:

$$k_{\psi} = -\frac{3p_m L_m \psi_s}{2L_s}, \quad (10)$$

where J_F is the generator's moment of inertia and p_m is the pole number of a doubly fed generator.

The output speed of the wind generator requires good tracking and anti-interference performances; it is also robust to the changes in system parameters. Most of the speed controllers designed by the EDM are PI controllers, making it difficult to simultaneously obtain good tracking and anti-interference performance. In this paper, a 3-DOF-IMC method is used to design the speed loop, and three controllers are used to adjust the tracking performance, anti-interference performance, and robustness of the speed loop.

5. The Principle of a 3-DOF-IMC

- (1) Decoupling effect: In the early stage, the 3-DOF-IMC was mainly used for the decoupling of a multivariable process control system, and in the late 1990s, it was applied to the decoupling of a motor model [27]. With the development of power electronics and power grid technology, the method of IMC decoupling has also penetrated into this field. For example, the cross-coupling problem of active and reactive power is solved in the PWM rectifier. Active and reactive currents are decoupled in flexible DC transmission systems, stationary synchronous series compensators and voltage source converters. The IMC decoupling method also has many application uses in a wind power generation system. The principle of the conventional IMC (1-DOF-IMC) decoupling is discussed in the reference, and the methods of the 2-DOF-IMC and 3-DOF-IMC decoupling and their applications in DFIG vector control are presented.
- (2) The multiple degrees of freedom IMC is used to achieve the independent regulation of multiple performance indexes of the control system.

The performance index of the control system includes tracking performance, anti-interference performance and robustness performance. The controller designed by the 1-DOF-IMC is difficult to achieve excellent tracking performance and anti-interference performance at the same time, which cannot meet the control requirements of a high-performance system. The 2-DOF-IMC can adjust the tracking performance and anti-interference performance of the system, respectively, and can mainly control the anti-interference performance of the system. However, when 2-DOF-IMC controllers are used to regulate the tracking performance and anti-interference performance, respectively, then the feedforward IMC controller needs to take both the anti-interference and robustness into account. In the 3-DOF-IMC, the given filter regulates the tracking performance of the system, the feedforward IMC controller mainly regulates the anti-interference performance, and the feedback filter regulates the robustness performance. From the research status, the 3-DOF-IMC is mainly used in the control system performance index regulation and dynamic decoupling. In addition to analyzing the tracking performance and anti-interference performance of the 3-DOF-IMC, this section also tries to use it to suppress the vibration of the drive train.

5.1. The Structure of a 3-DOF-IMC

The structure diagram of a 3-DOF-IMC is shown in Figure 11 [23].

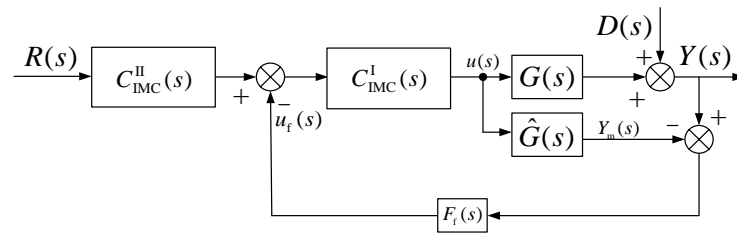


Figure 11. Block diagram of a 3-DOF-IMC.

In Figure 11, $C^I_{IMC}(s)$, $C^{II}_{IMC}(s)$, and $F_f(s)$ constitute a 3-DOF-IMC $F_f(s)$ that regulates the system’s robustness, $F_f(s)$, which is also known as a feedback filter. When $F_f(s) = 1$, the system degenerates to a 2-DOF-IMC with $C^{II}_{IMC}(s) = 1$. Then, the system is reduced to a 1-DOF-IMC. The following expression can be obtained according to Figure 11:

$$Y(s) = \frac{G(s)C^I_{IMC}(s)C^{II}_{IMC}(s)R(s)}{1 + C^I_{IMC}(s)F_f(s)[G(s) - \hat{G}(s)]} + \frac{[1 - F_f(s)\hat{G}(s)C^I_{IMC}(s)]D(s)}{1 + C^I_{IMC}(s)F_f(s)[G(s) - \hat{G}(s)]}. \quad (11)$$

When the controlled object matches the forecast model, i.e., $G(s) = \hat{G}(s)$:

$$Y(s) = \hat{G}(s)C^I_{IMC}(s)C^{II}_{IMC}(s)R(s) + [1 - F_f(s)\hat{G}(s)C^I_{IMC}(s)]D(s). \quad (12)$$

The 1-DOF-IMC method is used to design $C^I_{IMC}(s)$, where $C^I_{IMC}(s) = \hat{G}^{-1}_-(s)L_1(s)$, and controller $C^{II}_{IMC}(s) = \frac{L_2(s)}{L_1(s)}$ is selected. Since the decoupled system is approximately a first-order system, it is desirable that $F_f(s) = \frac{\alpha s + 1}{\beta s + 1}$. In the above correlation formula, α and β represent filter parameters of the filter $F_f(s)$. The internal model of the controlled object is $\hat{G}(s) = \hat{G}_+(s)\hat{G}_-(s)$.

5.2. The Analysis of the Tracking Performance and Anti-Interference Performance of a 3-DOF-IMC

According to Equation (12), the following expression can be obtained:

$$Y(s) = \hat{G}_+(s)L_2(s) \cdot R(s) + [1 - F_f(s)\hat{G}_+(s)L_1(s)] \cdot D(s). \quad (13)$$

The tracking and anti-interference performances of the system can be independently adjusted by changing the parameters of $L_1(s)$, $L_2(s)$, and $F_f(s)$.

5.3. The Robustness Analysis of a 3-DOF-IMC

The mechanical vibration of the wind drivetrain system will cause uncertainty in the generator model, which conforms to the multiplicative description of Equation (15) [22].

Usually, the controlled object containing uncertainty can be described in one of the following two ways:

- (1) Additive description:

$$G(s) = \hat{G}(s) + \Delta G(s) \quad (14)$$

- (2) Multiplicative description:

$$G(s) = \hat{G}(s)[1 + W(s)\Delta(s)] \quad (15)$$

Equations (14) and (15) are equal to each other, thus obtaining the following equation:

$$\Delta G(s) = \hat{G}(s)W(s)\Delta(s), \quad (16)$$

where $\|\Delta(j\omega)\|_\infty \leq 1$ and $W(s)$ is the weighting function that expresses the degree to which the uncertainty of the controlled object depends on the frequency ω .

The controlled object $G(s)$ in Figure 11 is expressed in the form of Equation (15), and its structure is transformed to obtain the equivalent structure in the dashed box, as shown in Figure 12. In this section, the robustness of an IMC system is mainly discussed. Therefore, only the influence of model uncertainty on the system characteristics is considered, while the influence of disturbance $D(s)$ on the system performance is temporarily neglected.

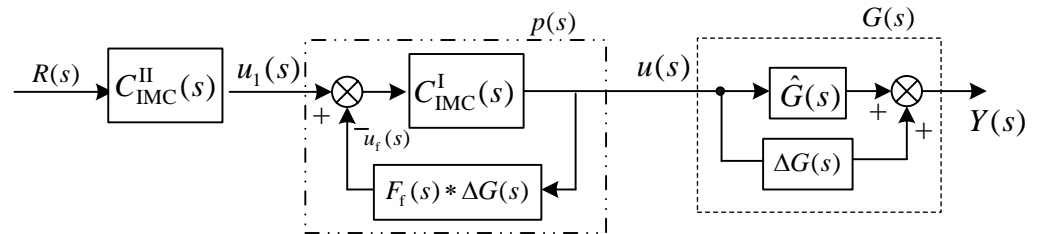


Figure 12. The equivalent open-loop block diagram of a 3-DOF-IMC.

The following relationships can be obtained according to Figures 11 and 12:

$$u_1(s) = C_{IMC}^{II}(s)R(s), \tag{17}$$

$$\frac{u(s)}{u_1(s)} = \frac{C_{IMC}^I(s)}{1 + C_{IMC}^I(s)F_f(s)\Delta G(s)}, \tag{18}$$

$$\begin{aligned} Y(s) &= G(s)u(s) = G(s)C_{IMC}^I(s)[u_1(s) - u_f(s)] = [\hat{G}(s) + \Delta G(s)]C_{IMC}^I(s)u_1(s) - G(s)C_{IMC}^I(s)u_f(s) \\ &= \hat{G}(s)C_{IMC}^I(s)u_1(s) + \Delta G(s)C_{IMC}^I(s)u_1(s) - G(s)C_{IMC}^I(s)u_f(s) \end{aligned} \tag{19}$$

$$u_f(s) = F_f(s)\Delta G(s).u(s) = F_f(s)\Delta G(s)\frac{C_{IMC}^I(s)u_1(s)}{1 + C_{IMC}^I(s)F_f(s)\Delta G(s)}. \tag{20}$$

Figure 11 can be equalized to Figure 12. Thus, the 3-DOF-IMC is an equivalent open-loop system.

5.3.1. The Robustness Stability Analysis of the 3-DOF-IMC

According to the IMC requirements, the parameters $C_{IMC}^{II}(s)$ and $G(s)$ are stable, as shown in Figure 12. Therefore, the necessary and sufficient condition for the stability of the open-loop control system shown in Figure 12 is that the local feedback unit $P(s)$ in the figure is stable. Furthermore, the necessary and sufficient conditions for $P(s)$ stability can be expressed as follows:

$$\left\| C_{IMC}^I(s)F_f(s)\Delta G(s) \right\|_{\infty} < 1. \tag{21}$$

Equation (16) can be substituted into Equation (22) to obtain:

$$\left\| C_{IMC}^I(s)F_f(s)\hat{G}(s)W(s)\Delta(s) \right\|_{\infty} < 1 \tag{22}$$

According to Figure 12 and Equation (22), the IMC system is an open-loop control. The zero poles of $C_{IMC}^{II}(s)$ and $G(s)$ can exactly counteract to achieve the system output tracking input given value. When uncertainty exists in the object model, the internal model of the object is introduced as $\hat{G}(s)$. The model uncertainty is separated from the object model. Then, the local feedback unit $P(s)$ is used. The feedback unit compensates to achieve robust control of the system.

The actual object may have a variety of structures. Regardless of the structure, the robust stability of the 3-DOF-IMC system is related to the feedback filter related to $F_f(s)$. Due to an import filter $F_f(s)$, $\left\| C_{IMC}^I(s)F_f(s)\Delta G(s) \right\|_{\infty}$ is lower than $\left\| C_{IMC}^I(s)\Delta G(s) \right\|_{\infty}$. Therefore, the degree of uncertainty $\left\| \Delta G(s) \right\|_{\infty}$ that the system will allow is higher than the disturbance from the outer environment.

5.3.2. The Robustness Performance Analysis of a 3-DOF-IMC

The system should be robust, stable, and characterized by good dynamic performance in engineering. The system should completely overcome the influence of the model uncertainty; hence, the following equation should be established according to Equation (19):

$$\Delta G(s) \cdot C_{IMC}^I(s) \cdot u_1(s) - G(s) \cdot C_{IMC}^I(s) \cdot u_f(s) = 0. \tag{23}$$

Substituting Equation (20) into Equation (23) yields:

$$C_{IMC}^I(s) \cdot u_1(s) \cdot \Delta G(s) \cdot \left[\frac{1 - F_f(s) \cdot C_{IMC}^I(s) \cdot \hat{G}(s)}{1 + C_{IMC}^I(s) \cdot F_f(s) \cdot \Delta G(s)} \right] = 0. \tag{24}$$

The sensitivity function $S = \frac{1 - F_f(s) \cdot C_{IMC}^I(s) \cdot \hat{G}(s)}{1 + C_{IMC}^I(s) \cdot F_f(s) \cdot \Delta G(s)}$ is then defined. The sensitivity function S 's value reflects the system's robust tracking performance. The smaller S is, the better the robust tracking performance.

Similarly, regardless of the structure of the controlled object, the robustness of the 3-DOF-IMC system is also related to the feedback filter $F_f(s)$, whose introduction decreases the sensitivity S and improves the robustness of the system.

6. The 3-DOF-IMC of Wind Generator Speed Loop

In this section, the MATLAB (2019b) simulation method is used to verify the tracking performance, anti-interference performance and vibration suppression ability of the IMC to control the DFIG. Compared with the system designed based on the EDM, the experiment proves the superiority of the 3-DOF-IMC method.

The dynamic structure diagram of the generator speed loop based on the 3-DOF-IMC is shown in Figure 13. The following parameters comprise Figure 13:

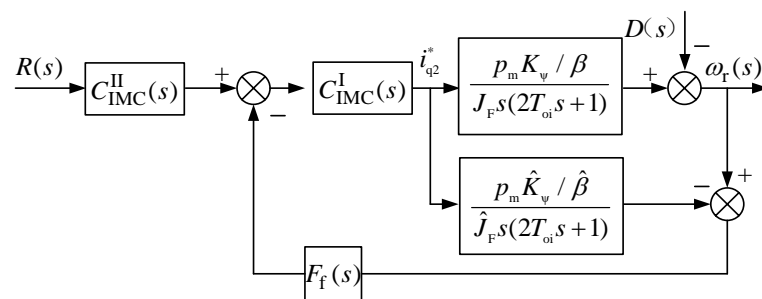


Figure 13. Dynamic structure of the speed loop based on the 3-DOF-IMC. * means the reference value.

- (1) The controlled object: $G(s) = \frac{p_m k_\psi / \beta}{J_F s(2T_{oi}s + 1)}$.
- (2) Internal model controller $C_{IMC}^I(s)$ designed via the 1-DOF-IMC method:

$$C_{IMC}^I(s) = G^{-1}(s)L_1(s) = \frac{J_F s(2T_{oi}s + 1)}{p_m k_\psi / \beta} \frac{2\lambda_{n1}s + 1}{(\lambda_{n1}s + 1)^2}. \tag{25}$$

$L_1(s)$ is introduced for the physical realization of the controller $C_{IMC}^I(s)$.

- (3) Internal model controller $C_{IMC}^{II}(s)$: If the filter $L_2(s) = \frac{2\lambda_{n2}s + 1}{(\lambda_{n2}s + 1)^2}$ is to be achieved, then the expression of the $C_{IMC}^{II}(s)$ should be obtained according to Equation (26):

$$C_{IMC}^{II}(s) = \frac{L_2(s)}{L_1(s)} = \left(\frac{\lambda_{n1}s + 1}{\lambda_{n2}s + 1} \right)^2 \frac{2\lambda_{n2}s + 1}{2\lambda_{n1}s + 1}. \tag{26}$$

- (4) Filter $F_f(s)$: $F_f(s) = \frac{\alpha s + 1}{\beta s + 1}$. The system output can be obtained according to Equation (13):

$$\begin{aligned} Y(s) &= \hat{G}_+(s)L_2(s) \cdot R(s) + [1 - \hat{G}_+(s)F_f(s) \cdot L_1(s)] \cdot D(s) \\ &= L_2(s) \cdot R(s) + [1 - F_f(s) \cdot L_1(s)] \cdot D(s) \end{aligned} \tag{27}$$

Since the controlled object contains no right-half plane zero, $\hat{G}_+(s) = 1$.

6.1. The Tracking Performance of the Wind Generator Based on $C_{IMC}^{II}(s)$

- (1) System simulation model

A 3-DOF-IMC simulation model of the wind generator speed loop is established according to the structure in Figure 13.

- (2) Simulation parameters

The parameters of the doubly fed wind generator used in the simulation are as follows: the moment of inertia J_F is $0.776 \text{ kg} \cdot \text{m}^2$, the polar logarithm P_m is 3, the constant K_Ψ / β is 0.388, and the filter time constant $T_{oi} = 0.001 \text{ s}$.

- (3) Model of the controlled object and the controller

The mathematical model of the controlled object can be expressed as:

$$G(s) = \frac{p_m k_\Psi / \beta}{J_F s (2T_{oi} s + 1)} = \frac{1.5}{s(0.002s + 1)} = \hat{G}(s). \tag{28}$$

- (4) Simulation waveform and conclusion

The given input is set to $40 \times 1 (t)$, the load disturbance input is $5 \times 1 (t-15)$, and the 3-DOF-IMC is adopted. The ratio of $\alpha/\beta = 1$ in the filter is kept constant, and three parameters (a), (b), and (c) in Table 2 are selected to obtain the tracking performance and anti-interference performance waveforms of the generator output speed, as shown in Figure 14a–c.

Table 2. Selection schemes and conclusions for the three parameters in Figure 14.

No.	λ_{n1}	λ_{n2}
(a)	0.01	0.5
(b)	0.01	1.2
(c)	0.01	2

Conclusion	When the parameter λ_{n1} is constant, the anti-interference performance is also constant	The tracking performance is improved with a decrease in parameter λ_{n2}
------------	---	--

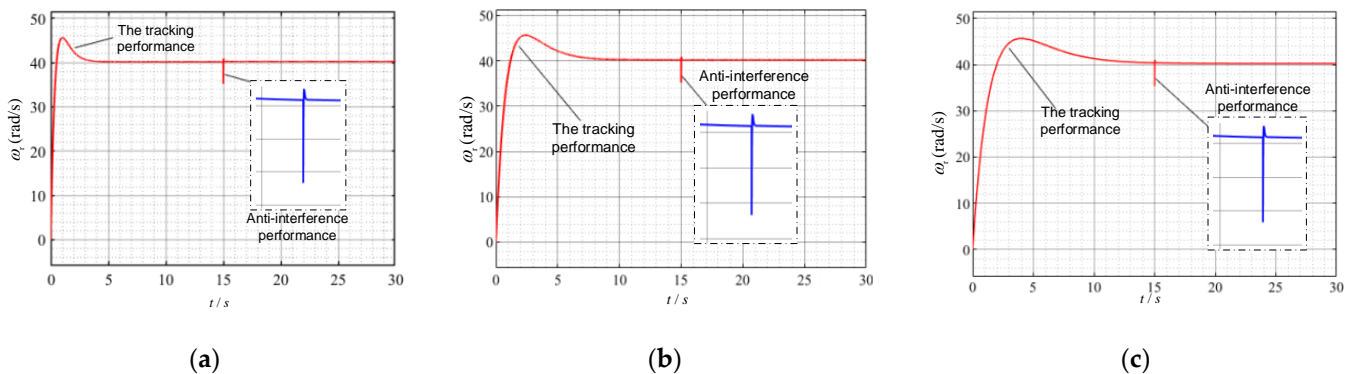


Figure 14. The output speed response curve of the system: (a) scheme (a); (b) scheme (b); (c) scheme (c).

The close-up of the anti-interference performance curve is shown in Figure 14. When the parameter λ_{n1} is constant, the anti-interference performance is also constant, while the tracking performance is improved with a decrease in the parameter λ_{n2} .

6.2. The Anti-Interference Performance of the Wind Generator Based on $C_{IMC}^I(s)$

Three parameter-selection schemes (a), (b), and (c) in Table 3 are taken for $\alpha/\beta = 1$ within the filter. It can be concluded that the waveform of scheme (a) is the same as that shown in Figure 14b. The tracking performance and anti-interference waveforms of the generator speed corresponding to schemes (b) and (c) are shown in Figure 15a,b.

Table 3. Selection schemes and conclusions for the three parameters in Figure 15.

No	λ_{n1}	λ_{n2}
(a) is the same as that of Figure 14b	0.01	1.2
(b)	0.08	1.2
(c)	0.64	1.2
Conclusion	When the parameters λ_{n1} are reduced, the anti-interference performance is improved	λ_{n2} is unchanged; hence, the tracking performance remains the same

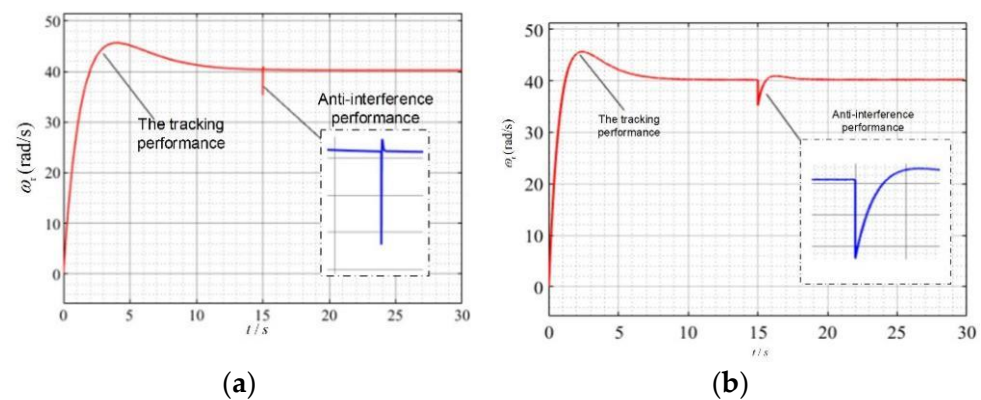


Figure 15. Output speed response curve of the system: (a) scheme (b); (b) scheme (c).

The close-up of the anti-interference performance curve is shown in Figure 15. It can be concluded that the anti-interference performance of the speed loop can be adjusted by modifying the parameter λ_{n1} . The parameters are small, and the anti-interference performance is good. When the parameter λ_{n2} is constant, the tracking performance is unchanged.

6.3. The Anti-Interference Performance of the Generator Based on the Feedback Filter $F_f(s)$

According to $Y(s) = L_2(s) \cdot R(s) + [1 - F_f(s) \cdot L_1(s)] \cdot D(s)$, the parameter $F_f(s)$ can also adjust the anti-interference performance of the generator speed with respect to the disturbance.

- (1) Anti-interference performance analysis of generator speed against step disturbance when parameters of $F_f(s)$ are changed.

The provided input $R(t) = 40 \times 1(t)$ and the disturbance input $D(t) = -5 \times 1(t - 20)$ are set, and a 3-DOF-IMC is adopted.

- (1) Two schemes (a) and (b) in Table 4 are employed to obtain the tracking performance and anti-interference performance waveforms of generator speed, as shown in Figure 16a,b. The close-up of the disturbance point waveform is indicated within the figure.

- (2) According to the anti-interference performance analysis, it can be concluded that the tracking performance of the speed loop is the same when the parameter λ_{n2} is unchanged. For the same parameter λ_{n1} , the maximum dynamic descent of the anti-interference performance remains constant. The recovery time varies with the value of α/β . The closer the value of α/β is to 1, the better the anti-interference performance.
- (2) Analysis of the anti-interference performance of generator speed to periodic disturbance signal when $F_i(s)$ is changed.

The following inputs are employed: $R(t) = 40 \cdot 1(t)$, and a load disturbance input in a periodic sine wave signal equal to $D(t) = 8\sin\omega t$. Lastly, a 3-DOF-IMC is also employed.

- (1) Two schemes (a) and (b) in Table 5 are considered to obtain the anti-interference performance waveforms of the generator speed to periodic disturbance signals, as shown in Figure 17a,b.
- (2) Anti-interference performance analysis: It can be concluded that different α/β values of the filter can affect the disturbance suppression ability of periodic disturbance signal. The closer the value of α/β is to 1, the stronger the ability of the system to suppress periodic disturbances.

Table 4. Two-step disturbance schemes and corresponding conclusions.

No	Tracking Performance		Anti-Interference Performance	
	λ_{n2}		λ_{n1}	α/β
(a)	1.2		0.08	1 ($\alpha = \beta = 1$)
(b)	1.2		0.08	0.5 ($\alpha = 0.5, \beta = 1$)
Conclusion	λ_{n2} is unchanged, tracking performance is unchanged		λ_{n1} is unchanged, the maximum dynamic descent of anti-interference performance is unchanged	
			The recovery time of anti-interference performance varies with the value of α/β	

Table 5. Two schemes and conclusions of periodic perturbation with sine wave signal.

No	Tracking Performance		Anti-Interference Performance	
	λ_{n2}		λ_{n1}	α/β
(a)	0.5		0.08	0.2 ($\alpha = 0.2, \beta = 1$)
(b)	0.5		0.08	1 ($\alpha = 1, \beta = 1$)
conclusion	When the value of α/β is close to 1, periodic disturbance suppression is improved.			

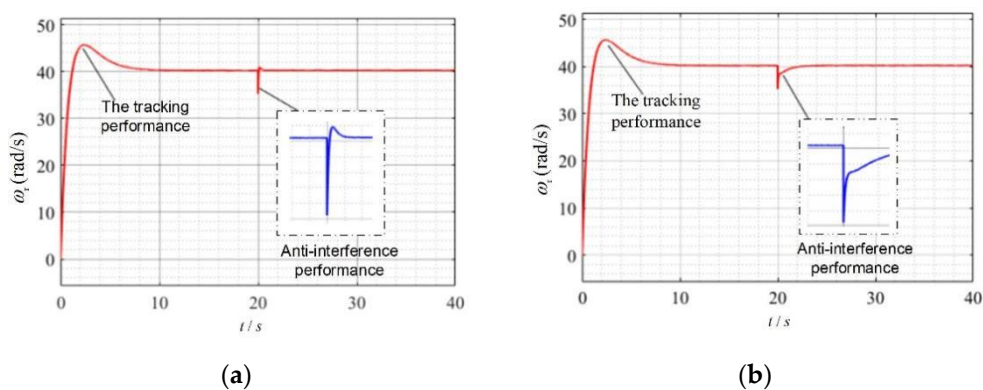


Figure 16. The output speed response curve of the generator when $F_i(s)$ is changed: (a) scheme (a); (b) scheme (b).

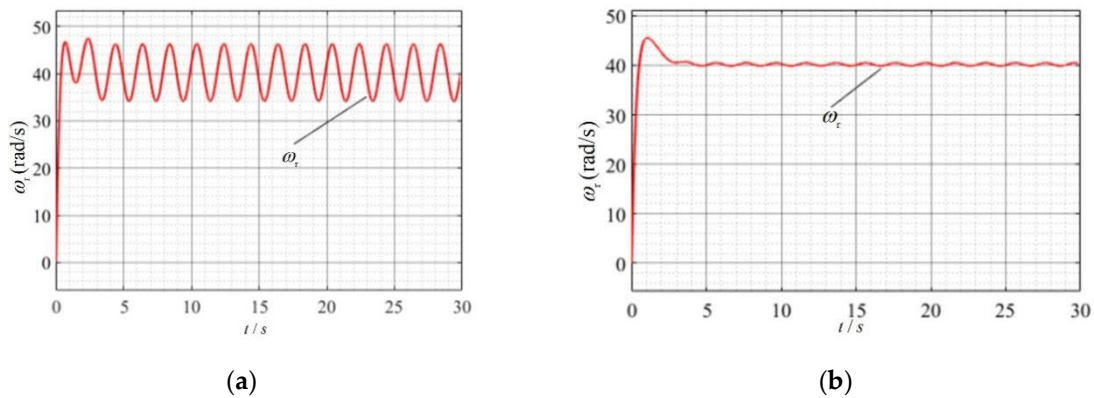


Figure 17. Output speed curve when the value of $F_f(s)$ changes: (a) scheme (a); (b) scheme (b).

6.4. Suppression of Drivetrain Vibration by Generator Speed Control Based on 3-DOF-IMC

Wind generator speed control based on the 3-DOF-IMC can suppress periodic disturbances, as demonstrated in Section 6.3. Moreover, generator speed vibration can be suppressed by adjusting the parameters of the filter $F_f(s)$. According to the analysis in Sections 2.3 and 2.4, the vibration waveform of the generator in the wind mechanical drivetrain system is also periodic. Therefore, the influence of the drivetrain vibration on the generator speed fluctuation can be eliminated by a 3-DOF-IMC of the wind generator.

Experimental Analysis of Drivetrain Vibration Suppression Based on the 3-DOF-IMC of Generator

The experimental simulation model of suppressing drivetrain vibration based on the 3-DOF-IMC is shown in Figure 18.

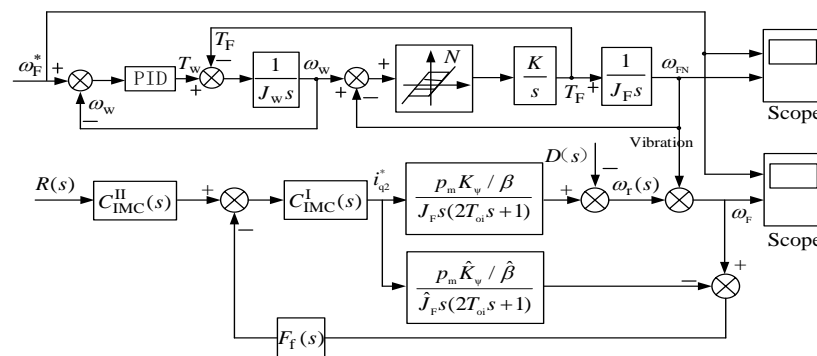


Figure 18. Experimental simulation model of drivetrain vibration suppression based on the 3-DOF-IMC of generator. * means the reference value.

Parameters of the two-mass drivetrain are taken from Table 3 in [5]. The 3-DOF-IMC generator parameters are described in this section. Furthermore, the effect of the $F_f(s)$ parameters on the system is discussed.

- (1) Analysis of the suppression of generator speed vibration for a variable $F_f(s)$ and constant $\alpha = \beta$ ratio.
 The input is set to $R(t) = 40 \times 1(t)$ and the 3-DOF-IMC is adopted. Two schemes (a) and (b) in Table 6 are taken to obtain the anti-interference performance waveforms of the generator speed to drivetrain vibration signals, as shown in Figure 19a,b. In the table, $\lambda_{n1} = 0.08$, $\lambda_{n2} = 0.5$, and $\alpha/\beta = 1$. However, the values of α or β are different. The vibration waveform of the two-mass drivetrain is shown in Figure 19a. The generator speed waveform with drivetrain vibration input signal is shown in Figure 19b.

- (1) According to the anti-interference performance analysis, it can be concluded that the optimal anti-interference performance of the drivetrain is obtained for the value of α/β equal to 1. Here, the output speed of the generator is not characterized by vibration.
- (2) Analysis of the suppression of generator speed vibration for a varying $F_f(s)$ parameter with respect to $\alpha \neq \beta$.
 - (1) Two schemes (a) and (b) in Table 7 are taken to obtain the anti-interference performance waveforms of the generator speed to drivetrain vibration signals, as shown in Figure 20a,b. In the table, $\lambda_{n1} = 0.08$, $\lambda_{n2} = 0.5$, and the α/β values are mutually different. The vibration waveform of the two-mass drivetrain remains constant, as shown in Figure 19a. The generator speed waveform with the drivetrain vibration signal is shown in Figure 20a,b.

According to the anti-interference performance analysis, it can be concluded that the disturbance suppression ability of $F_f(s)$ of the periodic disturbance signal differs when $\alpha \neq \beta$. The closer the value of α/β is to 1, the stronger the ability of the system to suppress periodic disturbances.

- (3) Analysis of generator speed vibration for the constant α/β ratio and modified values of α and β .
 - (1) Three schemes (a), (b), and (c) in Table 8 are considered to obtain the anti-interference performance waveforms of the generator speed to the drivetrain vibration signals, as shown in Figure 21a–c. The value of α/β is different for $\lambda_{n1} = 0.08$ and $\lambda_{n2} = 0.5$ in the table. However, the specific values of α and β are also different. The vibration waveform of the two-mass drivetrain remains constant. The waveform of the generator speed interference of the periodic vibration of the drivetrain is shown in Figure 21a–c.

Table 6. Two schemes and conclusions of periodic perturbation.

No	Tracking Performance	Anti-Interference Performance	
	λ_{n2}	λ_{n1}	α/β
(a)	0.5	0.08	1 ($\alpha = 0.5, \beta = 0.5$)
(b)	0.5	0.08	1 ($\alpha = 1, \beta = 1$)
Conclusion	The value of α/β is equal to 1, and good suppression of periodic disturbance is observed. The outputs of schemes (a) and (b) are the same.		

Table 7. Two schemes and conclusions of periodic vibration of drivetrain.

No.	Tracking Performance	Anti-Interference Performance	
	λ_{n2}	λ_{n1}	α/β
(a)	0.5	0.08	0.2 ($\alpha = 0.2, \beta = 1$)
(b)	0.5	0.08	0.8 ($\alpha = 0.8, \beta = 1$)
Conclusion	The closer the value of α/β is to 1, the better the suppression performance of the periodic disturbance.		

Table 8. Two schemes of periodic perturbation of drivetrain vibration with corresponding conclusions.

No.	Tracking Performance	Anti-Interference Performance	
	λ_{n2}	λ_{n1}	α/β
(a)	0.5	0.08	0.3 ($\alpha = 0.3, \beta = 1$)
(b)	0.5	0.08	0.3 ($\alpha = 0.12, \beta = 0.4$)
(c)	0.5	0.08	0.3 ($\alpha = 0.03, \beta = 0.1$)
Conclusion	Different values of α/β are characterized by different performance in suppressing periodic disturbances		

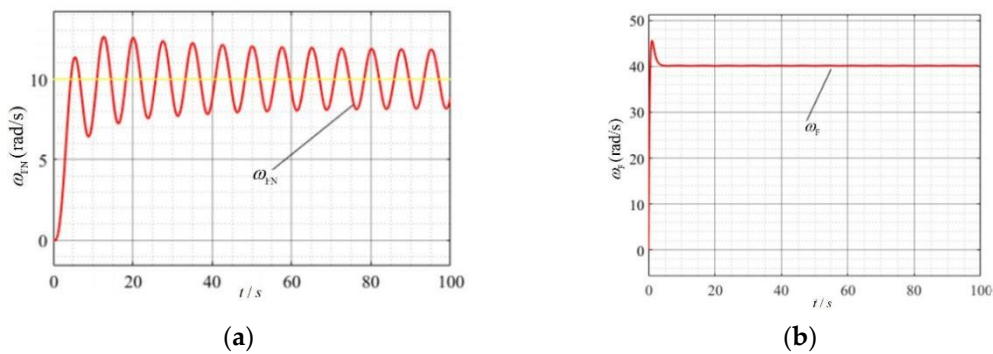


Figure 19. The output speed curve of the system for a variable $F_f(s)$: (a) two-mass drivetrain system vibration waveform; (b) generator speed curve. The yellow line is the reference value line.

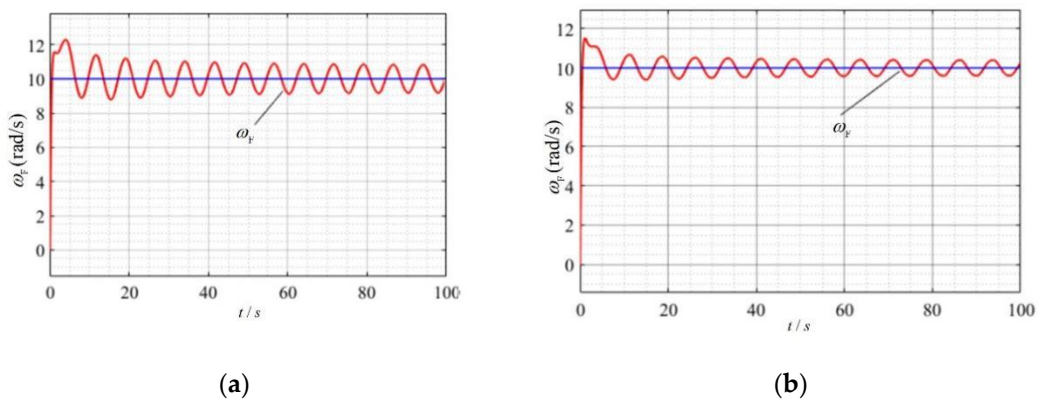


Figure 20. Output speed curve of the generator for varying $F_f(s)$ parameters: (a) scheme (a); (b) scheme (b). The blue line is the reference value line.

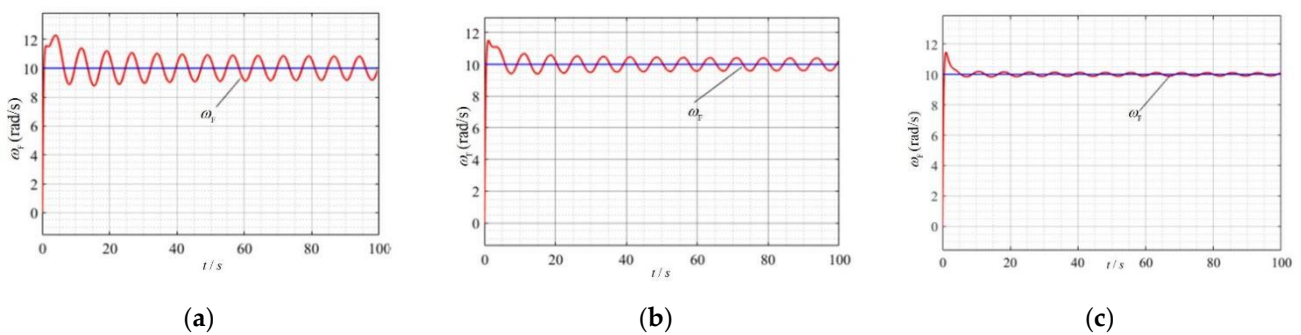


Figure 21. Output speed curve of the generator for variable $F_f(s)$: (a) scheme (a); (b) scheme (b); (c) scheme (c). The blue line is the reference value line.

According to the vibration suppression analysis, it can be concluded that different values of α and β have different effects on the suppression of generator speed vibration when $\alpha/\beta = 0.3$. The smaller the values of α and β , the smaller the speed vibration is, and the stronger the periodic disturbance suppression ability. This is because the smaller the values of α and β are, the smaller the influence of S in the transfer function $F_f(s)$ is, i.e., it is closer to 1.

6.5. The Vibration Suppression Ability Comparison of the 3-DOF-IMC and the EDM

- (1) Experimental scheme: The experimental scheme of the generator speed control is shown in Figure 22, and the drivetrain parameters are from Table 1. The speed detection and speed given signal have filtering parts.

The dashed box in Figure 22 is the speed loop, which is generally designed by the EDM, and the transfer function of the speed regulator ASR is chosen as

$$W_{ASR}(s) = k_n \frac{\tau_n s + 1}{\tau_n s} \tag{29}$$

where: K_n is the proportional gain of the speed controller; τ_n is the integration time constant of the speed controller.

By substituting Equation (10) into Figure 22, the small time constants T_{on} and $2T_{oi}$ are combined and approximated into an inertial part with a time constant $T_{\Sigma n} = T_{on} + 2T_{oi}$, so as to obtain the integral time constant of the speed controller

$$\tau_n = hT_{\Sigma n} \tag{30}$$

Gain coefficient of speed controller

$$k_n = \frac{J_F \beta}{\alpha p_m k_\psi} \cdot \frac{h + 1}{2hT_{\Sigma n}} \tag{31}$$

where: α is the feedback coefficient of speed, using unit feedback; h is the intermediate frequency bandwidth, which is generally set as $h = 5$ in engineering [28]. The generator moment of inertia J_F and parameters K_ψ / β have been defined previously.

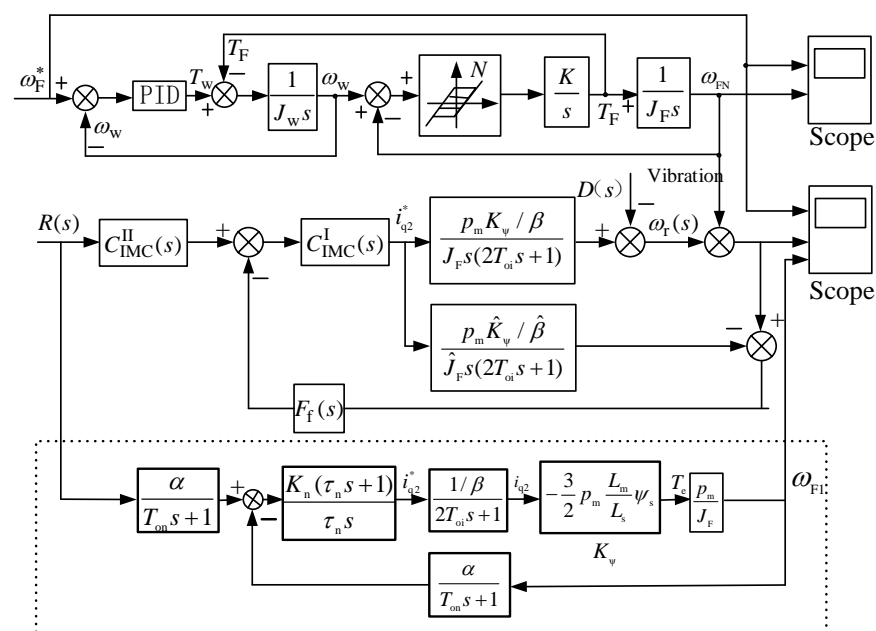


Figure 22. The experimental scheme of the generator speed control. * means the reference value.

Experimental results and analysis: The generator’s speed waveform is shown in Figure 23a, with parameters in scheme (a). Line 1 is the generator’s speed waveform based on the 3-DOF-IMC; Line 2 is the speed waveform based on the EDM; Line 3 is the reference speed waveform in the diagram. The generator’s speed waveforms of different values of α/β are shown in Figure 23b,c. In the figure, the parameters of the PI controller designed according to the EDM are shown in Equations (30) and (31), and its vibration amplitude overshoot is 5%; however, different values of α/β are characterized by different performances in suppressing periodic disturbances. With the increase in α/β , the overshoot of the vibration amplitude decreases. When $\alpha/\beta = 0.66$, the amplitude overshoot of the generator speed using the 3-DOF-IMC method is the same as the amplitude overshoot using the EDM. When $\alpha/\beta = 0.82$, the amplitude overshoot of the generator using the 3-DOF-IMC method is reduced to 50%. When $\alpha/\beta = 1$, the amplitude overshoot of the generator speed using the 3-DOF-IMC method is only 4% of the amplitude overshoot of the EDM, which is also a unit feedback, and the vibration amplitude of the 3-DOF-IMC method is greatly reduced. However, when the value of α/β is less than 0.66, the vibration suppression effect of the EDM is better than that of the 3-DOF-IMC method. In Table 9, the vibration suppression ability comparison of the 3-DOF-IMC and the EDM with corresponding conclusions is shown.

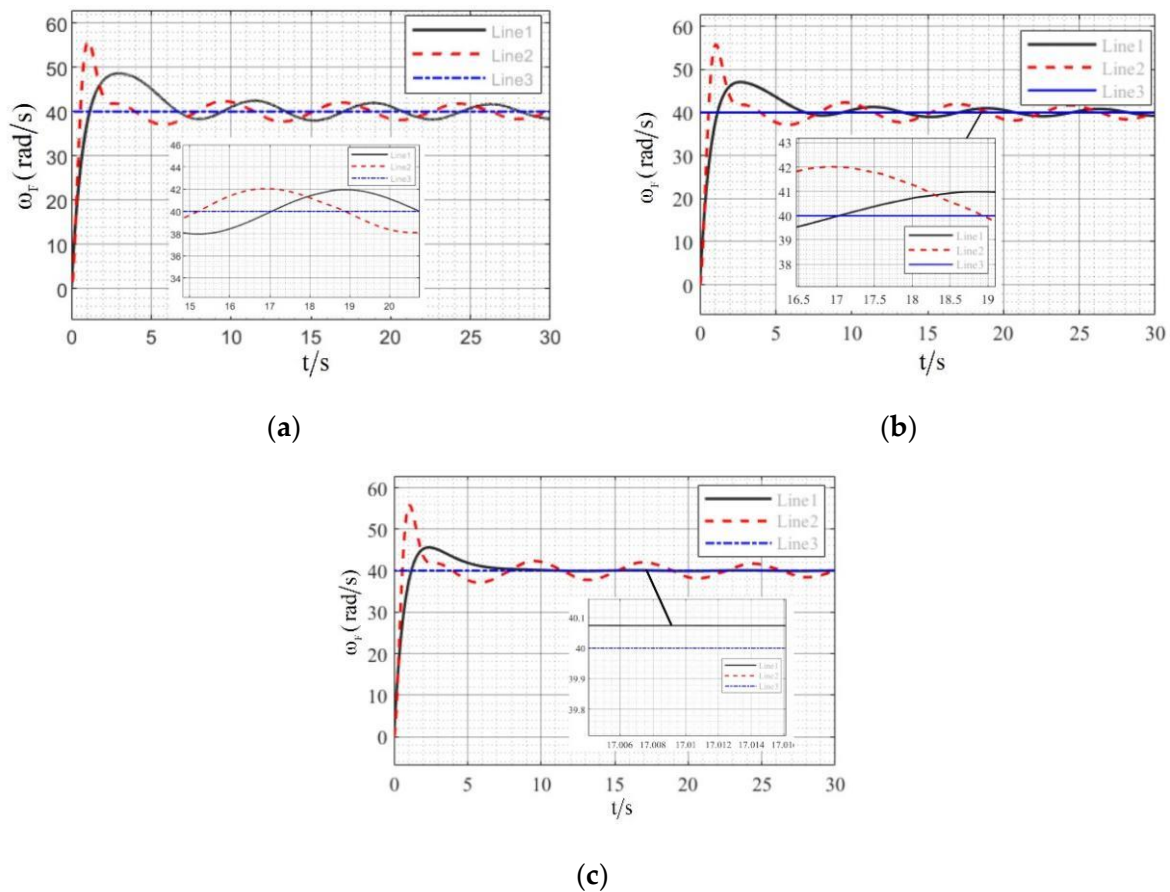


Figure 23. The vibration suppression ability comparison: parameters (a) scheme (a); (b) scheme (b); (c) scheme (c).

Table 9. The vibration suppression ability comparison of the 3-DOF-IMC and the EDM, with corresponding conclusions.

No.	3-DOF-IMC		Engineering Design Method (EDM)		
	α/β	Amplitude Overshoot σ_1	τ_n (Equation (30))	K_n (Equation (31))	Amplitude Overshoot σ_2
(a)	0.66 ($\alpha = 0.66, \beta = 1$)	5%	1	2	5%
(b)	0.82 ($\alpha = 0.82, \beta = 1$)	2.5%			
(c)	1 ($\alpha = 1, \beta = 1$)	0.2%			
Conclusion	Different values of α/β are characterized by different performance in suppressing periodic disturbances				

6.6. Generator’s Speed Tracking and Anti-Interference Performance Based on 3-DOF-IMC, Compared with EDM

- (1) Experimental scheme: The experimental scheme of the generator’s speed tracking and anti-interference performance based on the EDM is obtained according to reference [28]. Based on the EDM, the controlled object’s mathematical model can be expressed as Equation (32):

$$G_g(s) = \frac{p_m K_\psi}{J_F \beta s (T_{\Sigma n} s + 1)} = \frac{1.5}{s(0.2s + 1)}, \tag{32}$$

Thus, the integral time of the speed controller is $\tau_n = h T_{\Sigma n} = 1$; the gain coefficient of the speed controller is $k_n = \frac{J_F \beta}{\alpha p_m k_\psi} \cdot \frac{h+1}{2h T_{\Sigma n}} = 2$.

- (2) Experimental results and analysis: The generator’s speed waveform is shown in Figure 24. The solid Line-A in the figure is the generator’s output speed of the tracking performance and the anti-interference performance based on the 3-DOF-IMC. The dashed Line-B is the generator’s speed of the tracking performance and the anti-interference performance based on the EDM. The tracking and anti-interference performance controlled by the 3-DOF-IMC is better than that of the PI controller designed by the EDM.

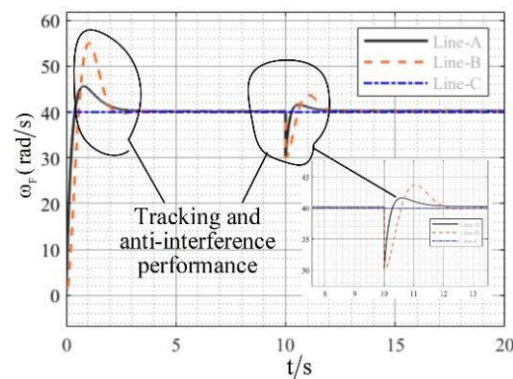


Figure 24. Generator’s speed tracking and anti-interference performance comparison.

6.7. Generator’s Speed Tracking and Anti-Interference Performance Based on 3-DOF-IMC, Compared with 1-DOF-IMC

- (1) Experimental scheme: The experimental scheme of the generator’s speed tracking and anti-interference performance based on the 1-DOF-IMC method is obtained according to reference [28], the mathematical model of the controlled object can be expressed as Equation (28).

The 1-DOF-IMC of the generator is as follows:

$$C_{\text{IMC-F}}(s) = G_{-}^{-1}(s)L(s) = \frac{s(0.002s + 1)}{1.5} \cdot \frac{1}{\lambda s + 1}$$

- (2) Experimental results and analysis: The generator's speed waveform is shown in Figure 25. The solid Line 1 in the figure is the tracking and anti-interference performance when the parameter λ is 0.4. The dashed Line 2 is the tracking and anti-interference performance of the generator's output speed when the parameter λ is 1.6. It can be seen that when the parameter λ is changed, the tracking and the anti-interference performance of the generator's speed change at the same time, which cannot be adjusted independently. However, the tracking performance and anti-interference performance controlled by the 3-DOF-IMC can be adjusted flexibly.

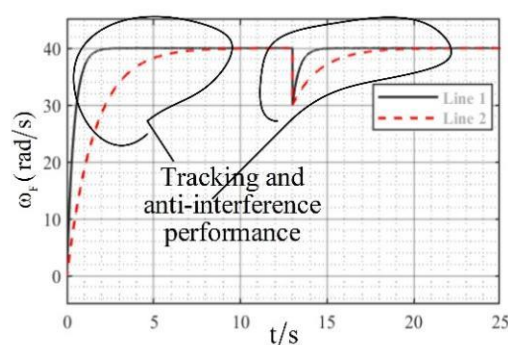


Figure 25. When the parameter λ is changed, the tracking and anti-interference performance of the generator's speed based on 1-DOF-IMC.

7. Conclusions

In this paper, the method of the suppression of vibration was proposed to adjust the aerodynamic torque of the wind turbine via variable pitch control and to control the electromagnetic torque and speed of the generator in order to suppress its speed vibration. Moreover, vector control and IMC were used for the doubly fed wind generator. A double closed-loop control scheme of wind generator speed based on 3-DOF-IMC was proposed. The following conclusions can be drawn:

The 3-DOF-IMC has three controllers with adjustable parameters and flexible adjustments that can independently control the tracking performance, anti-interference performance, and robustness performance of the wind generator speed loop.

The feedback filter has a suppression effect on the external periodic disturbance signal and can be used to suppress the periodic disturbance from the drivetrain. Thus, the influence of drivetrain vibration on the wind generator speed can be eliminated.

A 3-DOF-IMC plays an important role in decoupling the cross-coupling voltage of the generator. When the controlled object and forecast model are matched, the wind generator rotor resistance and inductance parameters are proportionally increased, reduced, or remain constant, and the decoupling effect of the 1-DOF-IMC is good. However, when the wind generator's rotor inductance and resistance parameters increase, decrease, remain constant, or change in reverse according to different proportions, the 1-DOF-IMC can hardly achieve full decoupling due to a lower number of adjustable parameters. Full decoupling can be achieved through multi-parameter coordination and by employing the 3-DOF-IMC. Further work is needed in the future.

Author Contributions: Conceptualization, C.Z.; methodology, C.Z.; software, Y.S.; formal analysis, C.Z.; investigation, Y.S.; resources, Y.S.; data curation, C.Z.; writing—original draft preparation, C.Z.; writing—review and editing, Y.S.; visualization, C.Z.; supervision, Y.S.; project administration, Y.S.; funding acquisition, Y.S. All authors have read and agreed to the published version of the manuscript.

Funding: This work was supported in part by the National Key research and development Program of China, No. 2020YFB1711102.

Institutional Review Board Statement: Not applicable.

Informed Consent Statement: Not applicable.

Data Availability Statement: The data that support the findings of this study are available from the corresponding author upon reasonable request.

Conflicts of Interest: The authors declare no conflict of interest.

References

1. Liu, H.; Tang, Q.; Su, Y.; Wei, L. A survey on electrical control methods of large wind turbine active vibration reduction. *J. Electr. Power Sci. Technol.* **2016**, *31*, 182–194.
2. Zhao, M.; Ji, J.C. Nonlinear torsional vibrations of a wind turbine gearbox. *Appl. Math. Model.* **2015**, *39*, 4928–4950. [[CrossRef](#)]
3. Zhao, M.; Ji, J. Dynamic analysis of wind turbine gearbox components. *Energies* **2016**, *9*, 110. [[CrossRef](#)]
4. Xing, Z.; Chen, L.; Xu, J.; Yang, Y. Torque Control Strategy Research of Large-Scale Wind Turbine. *Acta Energ. Sol. Sin.* **2012**, *33*, 738–744.
5. Xu, Z.; Pan, Z. Influence of Different Flexible Drive Train Models on the Transient Responses of DFIG Wind Turbine. In Proceedings of the 2011 International Conference on Electrical Machines and Systems, Beijing, China, 20–23 August 2011.
6. Chen, Z.; Zheng, L.; Xu, C. Stability and control of shaft torsional oscillation for doubly fed wind power generator. *Trans. China Electron Tech. Soc.* **2015**, *30*, 301–310.
7. Li, H.; Chen, Z. Transient Stability Analysis of Wind Turbines with Induction Generators Considering Blades and Shaft Flexibility. In Proceedings of the 33rd Annual Conference of the IEEE Industrial Electronics Society (IECON), Taipei, Taiwan, 5–8 November 2007.
8. Han, X.; Wang, P.; Wang, P.; Qin, W. Transient Stability Studies of Doubly-Fed Induction Generator using different Drive Train Models. In Proceedings of the 2011 IEEE Power and Energy Society General Meeting, Detroit, MI, USA, 24–28 July 2011.
9. Mohamed, A.; Abederrazek, L.; Lamine, M. PID Controller Design for a Wind Turbine with the Backlash Phenomenon. In Proceedings of the 2019 1st International Conference on Sustainable Renewable Energy Systems and Applications (ICSRESA), Tebessa, Algeria, 4–5 December 2019.
10. Sun, J. Control on Vibration of the Drive-Chain in wind turbines. *Drive Control* **2017**, *4*, 23–27.
11. Zhang, X.; He, W.; Hu, J. Impact of Inertia Control of DFIG-Based WT on Torsional Vibration in Drivetrain. *IEEE Trans. Sustain. Energy* **2020**, *11*, 2525–2534. [[CrossRef](#)]
12. Tian, W.; Pan, W.; Yang, S.; Liu, H. The Comprehensive Aerodynamic-Mechanical-Electrical Modeling of Doubly Fed Induction Generator Based Wind Turbine. In Proceedings of the 2020 Asia Energy and Electrical Engineering Symposium, Chengdu, China, 28–31 May 2020; IEEE: New York, NY, USA, 2020.
13. Xu, Z.; Wei, J.; Zhang, S.; Liu, Z.; Chen, X.; Yan, Q.; Guo, J. A state-of-the-art review of the vibration and noise of wind turbine drivetrains. *Sustain. Energy Technol. Assess.* **2021**, *48*, 101629. [[CrossRef](#)]
14. Y, Y.-Y.; Xuan, L.T.; Xin, L.D.; Liu, C.-Z. Natural Vibration Properties of a Wind Turbine Drivetrain. *Dev. Innov. Mach. Electr. Prod.* **2020**, *33*, 64–67.
15. Zhang, J.Y.; Li, J.; Du, X.; Xu, Y. Analysis on Torsional Vibration Response of Main Drive System of Wind Turbine Under Internal and External Mixed Excitation. *Mach. Des. Manuf.* **2020**, 25–30.
16. Wei, Y.; Yi, C.; Jie, Z. Vibration frequency tracking of wind turbine tower using paralleladaptive notch filter. *Acta Energ. Sol. Sin.* **2022**, *43*, 309.
17. Yang, L.; Yongsun, L.; Qiang, L. Research and Method Summary on Vibration Control of Wind Turbine Tower Structure. *SHIP Eng.* **2020**, *42* (Suppl. S2), 248–253.
18. Jia, Q.; Zhai, W.; Zhang, Q.; Sun, F.; Shen, M. Analysis of the influence of wind farms in full operating conditions on the torsional vibration of the shaft system of synchronous generators. In Proceedings of the 2021 International Conference on Power System Technology, Haikou, China, 8–9 December 2021.
19. Fitzgerald, B.; Basu, B. Vibration control of wind turbines: Recent advances and emerging trends. *Sustain. Mater. Struct. Syst.* **2020**, *4*, 347–372. [[CrossRef](#)]
20. Zhou, Y. Research on decoupling of cross-coupling voltage of doubly-fed wind turbine rotors. In Proceedings of the 27th Chinese Control Conference, Kunming, China, 16–18 July 2008.
21. Zhou, Y.; Zhu, X. Decoupling Control of the Rotor Cross-Coupling Voltage for Doubly-fed Induction Generator Based on Multiple Degree-Freedom Internal Model Control. In Proceedings of the 2010 Chinese Control and Decision Conference, Xuzhou, China, 26–28 May 2010.
22. Liu, H.; Ma, J. 2 DOF Robust Control for the Turntable Control Theory and Applications. *Tech. Autom. Appl.* **2007**, *26*, 4–7.
23. Zhou, Y.; Zhu, X. Application of Three-Degree-Freedom Internal Model Control and Mechanism Analysis of IMC System Robustness. In Proceedings of the 2009 Chinese Control and Decision Conference, Guilin, China, 17–19 June 2009; IEEE: New York, NY, USA, 2009.

24. Ling, Y. *Modeling, Simulation and Control of Doubly-Fed Wind Power System*; China Machine Press: Beijing, China, 2017; Volume 10.
25. Yang, M.; Hu, H.; Xu, D.G. Cause and suppression of mechanical resonance in PMSM servo system. *Electr. Mach. Control.* **2012**, *16*, 79–84.
26. Zhu, C.; Chen, S.; Ma, F.; Xu, X.; Xu, L.; Zhang, X. Effect of gear teeth modification on dynamic characteristics of a megawatt level wind turbine gearbox. *J. Vib. Shock.* **2013**, *32*, 123–128.
27. You, Q.; Wei, H.; Chang, X.; Tian, H. Flux-Weakening Control of PMSM Based on Three-Degree-of-Freedom Dynamic Internal Model Decoupling. *J. Unmanned Undersea Syst.* **2020**, *28*, 57–65.
28. Zhou, Y. *AC/DC Speed Regulating System and MATLAB Simulation*, 3rd ed.; China Electric Power Press: Beijing, China, 2020; Volume 10.